THE ASTROPHYSICAL JOURNAL, 839:68 (16pp), 2017 April 10 https://doi.org/10.3847/1538-4357/aa6a12

A Heuristic Approach to Remove the Background Intensity on White-light Solar Images. I. *STEREO*/HI-1 Heliospheric Images

Guillermo Stenborg and Russell A. Howard
Space Science Division, U.S. Naval Research Laboratory, Washington, DC 20375, USA
Received 2017 March 7; revised 2017 March 27; accepted 2017 March 27; published 2017 April 14

Abstract

White-light coronal and heliospheric imagers observe scattering of photospheric light from both dust particles (the F-Corona) and free electrons in the corona (the K-corona). The separation of the two coronae is thus vitally important to reveal the faint K-coronal structures (e.g., streamers, co-rotating interaction regions, coronal mass ejections, etc.). However, the separation of the two coronae is very difficult, so we are content in defining a background corona that contains the F- and as little K- as possible. For both the LASCO-C2 and LASCO-C3 coronagraphs aboard the *Solar and Heliospheric Observatory* (*SOHO*) and the white-light imagers of the SECCHI suite aboard the *Solar Terrestrial Relationships Observatory* (*STEREO*), a time-dependent model of the background corona is generated from about a month of similar images. The creation of such models is possible because the missions carrying these instruments are orbiting the Sun at about 1 au. However, the orbit profiles for the upcoming Solar Orbiter and Solar Probe Plus missions are very different. These missions will have elliptic orbits with a rapidly changing radial distance, hence invalidating the techniques in use for the *SOHO*/LASCO and *STEREO*/SECCHI instruments. We have been investigating techniques to generate background models out of just single images that could be used for the Solar Orbiter Heliospheric Imager and the Wide-field Imager for the Solar Probe Plus packages on board the respective spacecraft. In this paper, we introduce a state-of-the-art, heuristic technique to create the background intensity models of *STEREO*/HI-1 data based solely on individual images, report on new results derived from its application, and discuss its relevance to instrumental and operational issues.

Key words: methods: data analysis – Sun: corona – Sun: coronal mass ejections (CMEs) – techniques: image processing

1. Introduction

The brightness of the solar corona as seen in visible light (i.e., integrated along the line of sight), during an eclipse, for example, decreases with the distance to the Sun's center r. In particular, it decreases rapidly when close to the Sun by about r^{-8}, decreasing to about r^{-2} at distances above about 15 solar radii (Koutchmy & Lamy 1985). Above that height, the brightness continues as r^{-2} at least to the orbit of Earth (Leinert et al. 1998). The brightness arises from (1) radiation from some highly ionized elements, and (2) two sources of the scattering of light produced by the solar photosphere. The first component arises from the proper emission of highly ionized elements (e.g., iron, calcium, nickel) and is referred to as the emission corona (E-corona). In the visible region of the electromagnetic spectrum, this radiation comes from forbidden transitions, the brightest lines being Fe XIV and Fe X at 530.3 nm and 637.4 nm, respectively (e.g., Habbal et al. 2013). Their relative intensity to the continuum emission is negligible beyond $\sim 2.5\ R_\odot$. A second source of the white-light coronal brightness is due to scattering from free electrons in the coronal plasma (i.e., not from electrons bound to an ionic nucleus) in a process called Thomson scattering (e.g., Billings 1966). Due to the high coronal temperatures, the electrons move very rapidly, and hence the light dispersed by them loses any of the fingerprints from the photospheric spectrum (i.e., the Fraunhofer absorption lines). This component is hence referred to as the K-corona (the K letter stands for the German word *Kontinuerlich*, which means "continuum") to denote its continuum nature. The last source is due to scattering from dust particles, which are in orbit around the Sun and have different shapes, sizes, and composition (Leinert et al. 1998). Since the dust particles move much more slowly than the free electrons, the light dispersed by them keep the properties of the source (i.e., the presence of photospheric absorption lines). This third component thus is named the F-corona (the F letter stands for Fraunhofer). Beyond $\sim 2.5\ R_\odot$, these two sources (K- and F-corona) form the total coronal brightness. The relative contribution of each changes as a function of distance from the Sun. Close to the Sun, the electron scattering dominates. At around 5 $R_\odot$ (i.e., about $1^\circ\!.25$ elongation), they are about equal, and beyond this the dust dominates, being about 100 times brighter than the electron component out to Earth (Koutchmy & Lamy 1985).

The white-light corona, as it is more frequently called, has been observed from spaceborne satellites since 1971 (Howard 2006). Routine, continuous observations started in 1996 with the launch of the Large Angle Spectrometric Coronagraph (LASCO; Brueckner et al. 1995) on board the *Solar and Heliospheric Observatory* (*SOHO*; Domingo et al. 1995) into a halo orbit about the L1 point ($\sim 1.6 \times 10^6$ km from Earth, on the Sun–Earth line). Since 2006, the white-light imagers on board the twin spacecraft (S/C) of the *Solar Terrestrial Relationships Observatory* (*STEREO*; Kaiser et al. 2008) made possible the observation of the white-light corona (with the coronagraph instruments COR-1 and COR-2; Howard et al. 2008) and interplanetary medium (with the heliospheric imagers HI-1 and HI-2; Eyles et al. 2009), all the way to the Earth and beyond.

To reveal the dynamic K-coronal features of interest in the total brightness images, the background scene must be removed. The F-coronal part of the visible white-light corona is thought to be approximately constant on timescales of days or weeks, while the K-corona is highly dynamic. Both the *SOHO* and *STEREO* missions are orbiting about the Sun at about 1 au, in which the distance from the Sun varies slowly. This enabled us to develop empirical background images by taking the minimum of the daily median images over a period of 4 weeks, centered on the day of observation (Morrill et al. 2006). The daily median eliminates the short-term changes in the corona due, for example, to the passage of coronal transients such as coronal mass ejections (CMEs), and the monthly minimum eliminates the gradual changes in the scene, including stars. The background images established in this way have been quite successful. However, if a coronal structure is persistent for an entire solar rotation of 27 days, then an undesirable residual enhancement persists in the background image.

Straightforward techniques such as running- or base-difference schemes are in common use by the solar physics community if the primary interest is to reveal the rapidly moving (and sometimes extremely faint) coronal features. In these cases, the background scene is represented either by the corresponding image taken k minutes before or by a unique image taken at time $t_{\rm base}$, respectively (hereafter base image). Alternatively, the base image can be constructed as, for example, the time median of the images in a given (relatively short) time period. Although the static features are properly removed using this kind of approach (including both the stable dust component and the slowly moving K-corona features), the resulting frames are contaminated by the presence of dynamic structures at the time of the base frame. Therefore the proper interpretation of the resulting scene may be difficult, in spite of the approach being very effective in revealing rapidly varying structures.

To circumvent some of these caveats, several alternative methodologies have been proposed. For white-light coronagraph data, intensity-gradient filtering techniques (i.e., radial-graded filters) have been in use for a long time to remove the effect of the steep radial gradient of the coronal brightness. A straightforward implementation of this technique simply consists of subtracting the average intensity at a given height and dividing the difference by the standard deviation obtained in computing the average (the mapping of the image into a polar coordinate system is the most suitable representation for this purpose; see, e.g., DeForest et al. 2001; Morgan et al. 2006). Morgan & Habbal (2010) introduced the concept of dynamic separation, which is based on the least-squares fitting of quiescent coronal structures to polynomials. This idea was further developed by Morgan et al. (2012) for the removal of quiescent features. Briefly, the methodology consists in the separation of a sequence of images into quiescent and dynamic components by noting that at heights above $\approx 2.5\,R_\odot$, the quiescent component is nearly radial and changes slowly in time. The method involves iterating in a single image to find an approximation to the background and then deconvolving in the time dimension to obtain the background. More recently, Morgan & Druckmüller (2014) developed a new scaling technique called the Multi-scale Gaussian Normalization (MGN). In this technique, the image is rescaled by subtracting a Gaussian weighted local mean from the original intensity and then dividing the difference by the local standard deviation, also weighted by a Gaussian kernel. In this respect, it is similar to the technique devised in Morgan et al. (2006), except here a Gaussian kernel is used in the convolution. Finally the image is scaled by the arctan function, which is similar to a gamma function.

For removing the background intensity in the images obtained with the heliospheric imagers on board the twin S/C of the *STEREO* mission, DeForest et al. (2011) devised a technique to reveal solar wind structures and transient features in *STEREO*/HI-2 data. Because of the defocus problem with the *STEREO*/HI-2 instrument on *ST-B*, their work was restricted to data from *ST-A*. Briefly, the processing is performed in stages involving five major steps: removal of a stationary background (F-corona and stray light) formed by subtracting the minimum image of 11 days, removal of the star field, removal of the residual F-corona (a second-order effect), moving feature filtration in the Fourier plane, and conversion back to focal plane coordinates. The reader is referred to DeForest et al. (2011) for details of the procedure. The procedure has been adapted to work on *ST-A*/HI-1, *ST-A*/COR-2, and *ST-A*/COR-1 (see, e.g., DeForest et al. 2012; Howard & DeForest 2012).

The orbital characteristics of two upcoming missions—the Solar Orbiter (SolO; Mueller et al. 2013) and the Solar Probe Plus (SPP; Fox et al. 2016) missions—will not allow the use of techniques comprising several days worth of data to create the background images of the white-light imagers on board these missions (i.e., the Solar Orbiter Heliospheric Imager, SoloHI; Howard et al. 2013), and the Wide-field Imager for the Solar Probe Plus (WISPR; Vourlidas et al. 2013, 2016). In particular, for both the SolO and SPP missions, the background technique developed for *SOHO*/LASCO and *STEREO*/SECCHI involving the use of a month's worth of data will not work, because the radial distance is varying throughout the observing period. For example, during the 11 day perihelion pass, the SPP S/C will pass from 0.5 to 0.05 au and then back to 0.5 au in just 10 days. These perihelion distances will be closer to the Sun than ever before, and hence will open an entirely new spatial regime for dust observations. As the F-corona arises from the accumulation of dust scattering along the line of sight, at perihelion the line of sight will have a reduced path length and thus a reduced F-coronal contribution to the white-light images obtained with the respective instruments. Therefore it is desirable and convenient to obtain background images from at most a short interval of time to reveal the small fluctuations in the K-corona.

In light of this brief introduction, the goal of the current work was to explore new state-of-the-art algorithms to model the white-light background intensity and thus reduce as much as possible (or even eliminate) the F-corona contribution in heliospheric white-light images without relying on the use of images obtained over many days. As a result, a heuristic algorithm to model the background of individual *STEREO*/HI-1 images was developed. The paper is organized as follows. Section 2 describes the algorithm followed by a brief analysis of the residuals. Section 3 presents a photometric analysis of a synthetic CME to evaluate the photometric accuracy. Section 4 highlights new findings and characterizations made possible with this novel algorithm. Section 5 provides a discussion of the results and puts in perspective the applicability of the novel approach to present and new mission concepts. Finally, we conclude in Section 6.

2. The Algorithm

We developed a heuristic algorithm to model the background intensity in *STEREO*/HI-1 images out of individual images. The *STEREO* mission consists of two identically instrumented S/C in orbit about the Sun at about 1 au: one, *STEREO*-A (hereafter *ST-A*), drifting ahead of Earth, and the other, *STEREO*-B (hereafter *ST-B*), drifting behind Earth at a rate of $\sim 22^{\circ}\!.5$/year. Both S/C carried the Sun–Earth Connection Coronal and Heliospheric Investigation (SECCHI; Howard et al. 2008), which is a suite of five instruments designed to observe the expanding solar corona all the way from the Sun to the Earth and beyond. There are four white-light imagers in the *STEREO*/SECCHI suite: two coronagraphs (COR-1 and COR-2; Howard et al. 2008) and two heliospheric imagers (HI-1 and HI-2, Eyles et al. 2009).

The *STEREO*/HI-1 (hereafter ST/HI-1) instruments observe Thomson scattered light in the free electrons in the inner heliosphere from 4° to 24° elongation (Eyles et al. 2009), with a nominal cadence of 40 minute. The background intensity in ST/HI-1 images is formed by the contribution of two components. Namely, (i) the stable F-corona, and (ii) instrumental effects. Instrumental effects include a diffracted stray-light component and ghost images, as well as intensity patterns that arise from both dust in the optics and artifacts in the detector produced in the fabrication process. The stray-light component is expected to be a function of the radial distance between the S/C and the Sun (i.e., due to the changes in the apparent size of the Sun). Finally, S/C off-pointing from Sun-center can also affect the diffracted light pattern imaged onto the focal plane.

The core of the technique devised relies on the spatial frequency characteristics of the intensity component to be modeled. It consists of two main stages, both containing several steps. The first stage (hereafter Stage 1, Section 2.1) is aimed at finding a rough estimation of the background intensity level along each individual row of the image. The individual row background models obtained in this stage are contaminated by remnant K-coronal structures. Their presence is minimized with the second stage of the algorithm (hereafter Stage 2, Section 2.2).

In the following, a detailed descriptive account of the technique is presented. The analysis of the residuals is addressed in Section 2.3. The description is based on a particular example (an *ST-A*/HI-1 image taken on 2011 June 25). Note that the algorithm remains the same for *ST-B*/HI-1 and for *ST-A*/HI-1 after *ST-A* passed behind the Sun, but in these cases, the images must be rotated 180° to place the Sun on the right. Hence, by obtaining a similar intensity profile to the example shown here, the functional form of the analytical models proposed remains valid. We expect that when *ST-B* is recovered after passing from behind the Sun, it will also be treated in the same way as *ST-A*/HI-1 is now.

2.1. Stage 1

In Stage 1, the technique computes a first-order background model by fitting the intensities along each row of the image to an ad hoc parameterized function. Let I_j be the intensity profile of a calibrated *ST-A*/HI-1 image at row j. The calibration of *ST-A*/HI-1 images is performed with the *secchi_prep* command of the IDL Solarsoft (SSW) package. The first step consists of fitting the intensity profile I_j with an ad hoc analytic model of the intensity profile along that row. Note that the domain of the function representing the analytical model is not along a radial direction. There is a certain degree of freedom on the analytical model to be chosen, as long as the model complies with certain criteria. These criteria are established to force the model to mimic the mathematical characteristics of the expected profile of the F-corona plus stray light along each row. Namely, (i) the analytical model must increase monotonically (from large to smaller elongations) in the whole domain (i.e., its first derivative must be strictly positive), and (ii) its second derivative must be strictly positive in at least a restricted domain comprising the range between the 10th and 90th percentile (i.e., excluding the edges of the field). The latter constrains the model to have its first derivative increase monotonically in the subdomain (border effects are unavoidable).

For the example presented here, we fit the intensity profile at each row (I_j) with the analytical model given by the expression

$$I_j^{[0]} = \frac{c_0^j}{c_1^j + c_2^j \cdot x^{c_3^j}}, \tag{1}$$

where x denotes the pixel position, and c_i^j ($i = 0 \ldots 3$) are the coefficients of the model for row j, which are obtained by a nonlinear least-squares fit of I_j to the supplied function. The superscript 0 is simply used to differentiate the model from the signal. For illustration purposes, the left panel of Figure 1 shows the ratio between the intensity profile I_{400} and the fitted model $I_{400}^{[0]}$ (black curve). As seen in the example, the model may not fit perfectly the intensity profile. Therefore the ratio $I_j/I_j^{[0]}$ may not be free of artifacts. For instance, the black curve highlights a couple of very low frequency oscillations resulting from a non-perfect fitting of the model. The goal in the remaining steps is to reduce the oscillations and form the model of the background.

To reduce the magnitude of this error, we define the following correction factor α_j:

$$\alpha_j = \frac{I_j}{I_j^{[0]}} \otimes K, \tag{2}$$

where the symbol $\otimes$ is used to denote the mathematical operation *convolution*. The kernel K is chosen as the kernel of a Savitzky–Golay smoothing filter (Savitzky & Golay 1964) of degree 2 (kernel's size of 190 pixels for the 1024 × 1024 image of the example presented here). The correction factor α_j is simply a smoothed version of the ratio between the original signal I_j and the model $I_j^{[0]}$ from Equation (1). In Figure 1 (left panel) we have over-plotted in red the correction factor α_{400}. As illustrated, the factor preserves the very low spatial frequencies (i.e., large, smooth features, as for example, the error introduced by the bad fitting), and reduces (but does not eliminate) the relative intensity and noise of the signal at high and mid frequencies (due, e.g., to CME fronts, co-rotating interaction regions, intensity inhomogeneities embedded in the solar wind, and large-scale streamers). Note that the kernel's size is a free parameter: a smaller kernel's size, for example, will result in smaller discrete K-coronal structures being preserved in the factor.

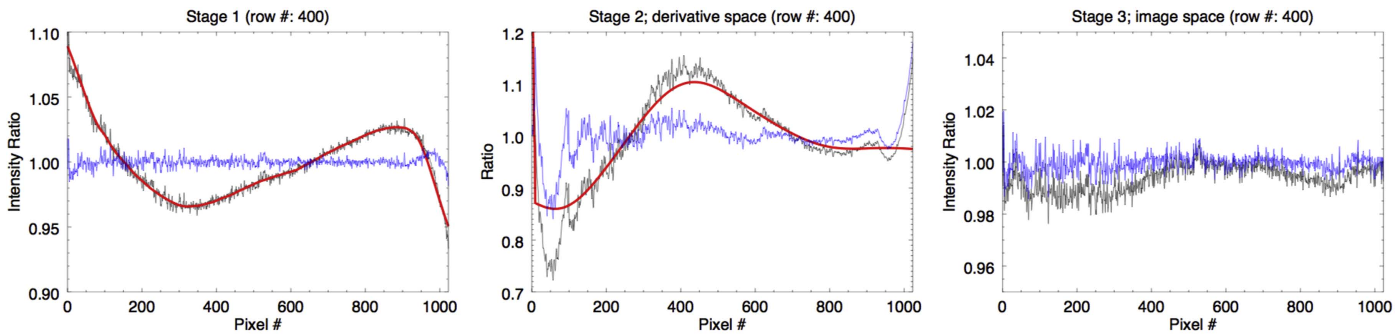

Figure 1. Illustration of the background model determination for row 400 of the *ST-A*/HI-1 (calibrated) image taken on 2011 June 25 at 10:09 UT. Left panel: Stage 1. The black curve depicts the ratio between the intensity profile I_{400} and the analytical model proposed in Equation (1) (i.e., $I_{400}^{[0]}$); the red curve delineates the α_{400} factor (Equation (2)); and the blue curve represents the ratio between the intensity profile I_{400} and the first-order model $I_{400}^{[1]}$ (Equation (3)). Middle panel: Stage 2 (derivative space). The black curve depicts the ratio between the derivative of the intensity profile of the first-order background model $I_{400}^{[1]}$ and the analytical model proposed in Equation (4) (i.e., $z_{400}^{[0]}$); the red curve delineates the β_{400} factor, which was obtained with a multi-resolution based smoothing algorithm; and the blue curve represents the ratio between the derivative of the first-order model $I_{400}^{[1]}$ and the corrected model $z_{400}^{[1]}$ (Equation (5)). Right panel: Stage 2 (image space). The black curve delineates the ratio between the intensity profile I_{400} and the second-order model $I_{400}^{[2]}$ (which results from the integration of Equation (5)); and the blue curve depicts the ratio between I_{400} and the third-order model $I_{400}^{[3]}$ (Equation (6)).

By applying this correction factor, the first-order background model becomes

$$I_j^{[1]} = \alpha_j \cdot I_j^{[0]}. \tag{3}$$

By multiplying $I_j^{[0]}$ by the correction factor α_j, we reduce the error introduced by the bad fitting, while still preserving the intensity gradients characteristic of discrete K-coronal structures (although at a different intensity level). Note that depending upon the size of the kernel, certain (small) discrete K-coronal structures might be eliminated. The green curve in Figure 1 (left panel) depicts the ratio $I_{400}/I_{400}^{[1]}$, which clearly shows that the error introduced by the bad fitting is greatly reduced when the correction factor is applied.

2.2. Stage 2

As discussed previously, this first-order estimate of the background $I_j^{[1]}$ (Equation (3)) may still be contaminated by remnant intensity bumps resulting from discrete K-coronal features not properly eliminated. To minimize their presence, stage 2 applies a filter to remove the remnant high and mid frequencies from $I_j^{[1]}$. The simplest approach would be to apply a low-pass filter. However, given its monochromatic character, a simple low-pass filter is not appropriate in this case. Therefore in Stage 2 we make use of a multi-resolution technique to filter out the effect of the undesired features.

Since the features to be removed are embedded in a smooth background with a relative intensity of the same order, it is more suitable to work in the gradient space. Let z_j be the derivative of the first-order model $I_j^{[1]}$. As in stage 1, we fit z_j with a new ad hoc analytical model, which must also follow the mathematical constrains established before. For the example presented here, we chose

$$z_j^{[0]} = b_0^j \cdot (b_1^j)^{b_2^j \cdot x} + b_3^j, \tag{4}$$

where x denotes the pixel position, and b_i^j ($i = 0...3$) are the coefficients of the model for row j, which were obtained by a nonlinear least-squares fit of z_j to the supplied function. We illustrate this part of the procedure in the middle panel of Figure 1: the black curve delineates the ratio between the derivative of the intensity profile of the first-order background model $I_{400}^{[1]}$ (i.e., z_{400}) and $z_{400}^{[0]}$. As in stage 1, the model $z_j^{[0]}$ may not fit perfectly z_j (note the big oscillation that the curve exhibits around the mean value of 1). To minimize the effect of the bad fitting, it is again necessary to define a correction factor (β_j). However, this time we want the correction factor β_j to account only for the error introduced by a non-perfect fitting of the analytical model chosen (Equation (4)). This can be achieved by means of a multi-resolution filtering technique.

The correction factor β_j is computed by applying a wavelet-based smoothing/cleaning algorithm to the ratio $z_j/z_j^{[0]}$. The multi-resolution smoothing/cleaning algorithm used is a customized 1D-version of the algorithm described in Stenborg et al. (2008). Since we are not interested in a fine frequency partition, we implemented the algorithm via the $\acute{a} - trous$ discrete wavelet transform (WT) instead of the continuum WT to reduce the number of iterations necessary to get the background level of the signal and hence make it computationally faster. Because of the properties of the multi-resolution methodology, β_j follows well the eventual oscillation (very low frequency) introduced by a bad fitting of the model proposed, while filtering out the mid- and high-frequency content of the signal (e.g., the signal resulting from CME fronts and streamer crossings not properly accounted for in stage 1). The red curve in the middle panel of Figure 1 shows the correction factor β_{400} for the example under consideration.

Then, by multiplying the resulting model $z_j^{[0]}$ by the correction factor β_j, we obtain a model $z_j^{[1]}$ of the derivative of $I_j^{[1]}$ (Equation (5)):

$$z_j^{[1]} = \beta_j \cdot z_j^{[0]}. \tag{5}$$

The green curve on the middle panel of Figure 1 shows the ratio $z_{400}/z_{400}^{[1]}$ to illustrate the goodness of the fit. There are, however, noticeable border effects. We are exploring techniques to address this issue, particularly at the sunward side.

To apply this to the first-order background image, we simply integrate $z_j^{[1]}$ to obtain the second-order background model $I_j^{[2]}$. The nonlinear filter applied in the gradient space might have introduced undesired effects, some of which may have not been fully addressed with the correction factor β_j. To illustrate this, we plot in the right panel of Figure 1 the ratios $I_{400}/I_{400}^{[2]}$ (black curve). In this example, we note that the second-order background model $I_j^{[2]}$ overestimates the mean signal value

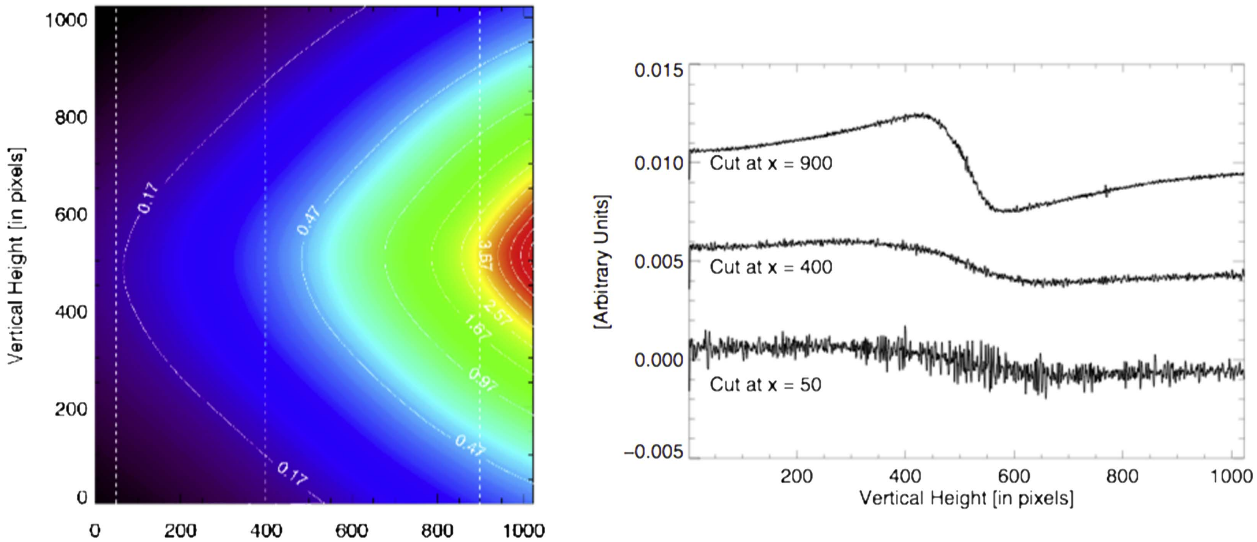

Figure 2. Left panel: background model obtained for the *ST-A*/HI-1 (calibrated) image taken on 2011 June 25 at 10:09 UT (in 10^{-11} calibrated intensity units). Right panel: derivative of the intensity profile at the locations indicated by the dashed vertical lines in the image on the left panel.

on both the left and the right sides of the image. This issue can be easily corrected, along with the removal of any remnant intensity bumps (which are the signature of the discrete K-coronal features we were intending to remove from $I_j^{[1]}$) by defining a new correction factor γ. This factor γ is computed in a similar fashion to β (i.e., by using a wavelet-based smoothing/cleaning algorithm to the ratio ratio $I_j^{[1]}/I_j^{[2]}$). In this way, we obtain the third-order background model $I_j^{[3]}$ for each row as

$$I_j^{[3]} = \gamma_j \cdot I_j^{[2]}. \quad (6)$$

The ratio $I_{400}/I_{400}^{[3]}$ is depicted with the green curve in the right panel of Figure 1.

2.3. On the Algorithm Performance

The procedure devised treats each row independently. The only connection between adjacent rows is that the analytical models parameters found for row j (i.e., $c_i^{[j]}$ and $b_i^{[j]}$, with $i = 1, 2, 3$) are given as initial guesses to find the analytical model parameters for the next row. This scheme leads to small variations from row to row of the overall intensity level. As will be shown next, the relative intensity variation is negligible for practical purposes.

The background model obtained for the test image provided previously is shown in the left panel of Figure 2. The derivative of the normalized intensity profiles of the background model at the locations indicated by the vertical dashed lines is shown in the right panel. (For a proper comparison, we normalized each intensity profile by its maximum.) The corresponding profiles at pixel locations $x = 400$ and $x = 900$ are shifted by 0.005 units to help compare them. The plots show that the relative intensity variation from row to row are of the order of 0.1% (when the SNR is low) and decrease in the sunward direction.

To assess qualitatively how much remnant K-coronal signal is present in a given background model (a more quantitative analysis is carried out in Section 3), we show in Figure 3 the intensity ratio between the background models obtained with our algorithm for the *ST-A*/HI-1 images taken on 2011 June 25 at 10:09 UT and 00:49 UT. The diffuse, brighter pattern around the center of the image is a remnant signature of the front of a CME (relative residual intensity $<1\%$ for the example considered here). The pattern observed at large elongations is the artifact, due to the relative intensity variation from row to row, which becomes noticeable when the SNR is very low.

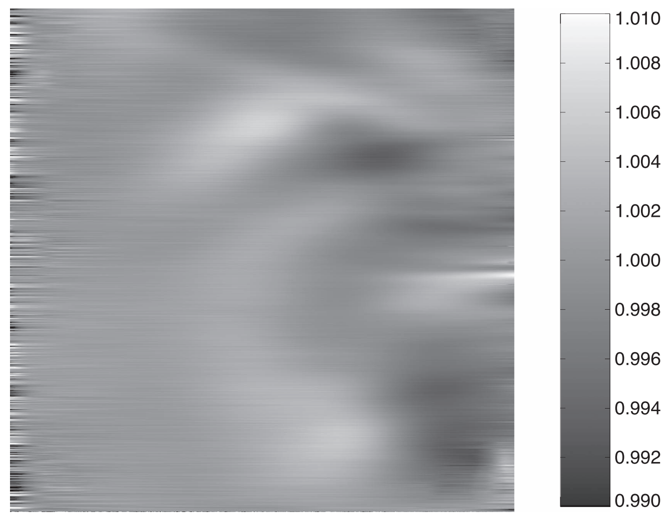

Figure 3. Intensity ratio of the background models of the *ST-A*/HI-1 images taken on 2011 June 25 at 10:09 UT and 00:49 UT.

At this point, we ask ourselves: does this new approach to compute the individual intensity background models of ST/HI-1 data help shed light on new scientific insights? In Figure 4 we show five snapshots to help answer this question (more detailed examples are shown in Section 4). The panel (a) of Figure 4 shows the difference between two *ST-A*/HI-1 calibrated images taken on 2011 June 25, with 10 hr difference (10:49 UT and 00:49 UT), where, in particular, a faint and diffuse CME front can be seen under development. The big time gap between the images was chosen to prove our point. The panel (b) of Figure 4 shows the difference between the corresponding background-normalized images, with the residual added (see Figure 3). We have used the same intensity thresholding to display both snapshots. In spite of the faintness and diffusiveness of the K-corona dynamic feature, we notice

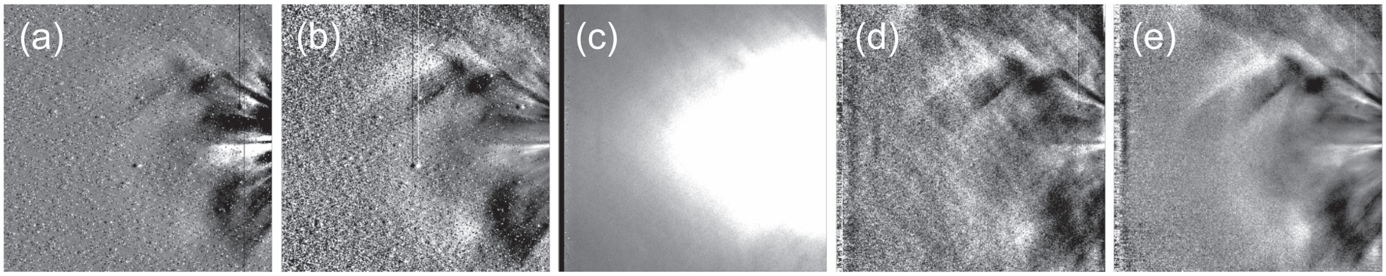

Figure 4. Snapshots obtained as the difference between two *ST-A*/HI-1 images taken on 2011 June 25 at 10:49 UT and 00:49 UT. Panel (a): straight difference between the calibrated images. Panel (b): straight difference between the background-corrected calibrated images (residual added). Panel (c): straight difference between the calibrated images, the base image being shifted to account by the star field displacement. Panel (d): straight difference between the background-corrected calibrated images, the base background ratio image being shifted to account by the star field displacement (residual added). Panel (e): same as panel (d), corrected with a model of the instrument artifacts. All snapshots have been intensity-thresholded at the same level.

its higher intensity contrast with respect to the background (and thus better visibility).

As can be seen in panels (a) and (b) of Figure 4, the visibility of the faint coronal features is highly obscured by the star field when using a running-difference scheme to reveal the dynamic features. A common technique in use with the data from the *STEREO* heliospheric imagers is to shift (before subtraction) the base image to match the star field of the other image. A straightforward application of such an approach on the two calibrated images of our example is shown in panel (c) of Figure 4. It is clear that without removing the background intensity, the shifting of the base image produces an undesired effect (of particular importance if the time gap between the images is large). Therefore, by normalizing the images by their (individual) backgrounds prior to the differencing, this issue becomes irrelevant, as can be seen in panel (d) of Figure 4. However, nothing is for free: we note in this snapshot the appearance of several features of instrumental nature (e.g., a pattern of circular "saw" marks among others; they are discussed in detail in Section 4.1.2). As will be shown in Section 4.1.2, it is possible to empirically model these artifacts. Then, by applying this model to each background-normalized image prior to differencing, the difference frame can be obtained free of instrumental artifacts. This is shown in panel (e) of Figure 4.

3. Photometric Analysis

To check on the photometric characteristics of the ST/HI-1 images processed with the background models created with our technique, we used a set of 30 synthetic images with a pre-defined, calibrated CME event (starting in the second image) embedded in a zero intensity background (see Wood & Howard 2009). To simulate real conditions, each instance of the CME model of excess brightness was in a form such that it could be added to a *ST-A*/HI-1 calibrated image. Therefore, to create the test set, we added the set of 30 synthetic images to a corresponding set of consecutive *ST-A*/HI-1 (calibrated) images taken with a 40 minute cadence during a time period characterized by the absence of relatively large, discrete K-coronal dynamic features (i.e., on 2011 Jan 15 between 00:09 UT and 19:29 UT).

The top row of Figure 5 shows four time instances of the original, synthetic CME event (hereafter S_t, $t = 1, 2, 3, 4$). The time label indicated on each panel corresponds to the time of the *ST-A*/HI-1 image, where the time instance of the synthetic event was then added to create the test set.

We applied our algorithm to the test set to create the corresponding background models. Each background model was then subtracted from the corresponding test image to create a set of excess brightness images. As briefly shown at the end of Section 2.3, each *ST-A*/HI-1 image treated with its own background reveals instrumental artifacts resulting from the fabrication process and/or optics, which obscure the faint K-coronal signal of interest. To reduce the magnitude of this undesired effect and thus allow for a better quantitative analysis, we created a rough model of the instrumental artifacts by taking the time median of the 30 excess brightness images. The validity of this procedure is shown in Section 4.1.2. The second row of Figure 5 shows the corresponding excess brightness images corrected by the model of the instrumental artifacts (hereafter B_t). The synthetic CME event is clearly seen, although its absolute intensity value is apparently not fully recovered.

The snapshots in the third row of Figure 5 show the results obtained (hereafter K_t) after adding the residuals to each B_t. The residuals were simply obtained by adding to each image the excess brightness of each background model with respect to the time median of the 30 background models of the test set. Finally, the bottom row of Figure 5 shows the result of subtracting the synthetic CME (set S_t) from the corresponding K_t set (hereafter F_t), highlighting the recovery of the K-coronal signal in the original *ST-A*/HI-1 images used for this exercise.

Both the star field and the resulting excessive noise in the snapshots of B_t, K_t, and F_t make it difficult to compare quantitatively the intensity levels of the original and recovered CME signal. Therefore, we first proceeded to diminish the effect of the star field by subtracting to each time instance of B_T, K_t, and F_t, the first processed image of the corresponding set (i.e., B_0, K_0, and F_0, respectively), after shifting them by a given amount of pixels to match the star field in the corresponding image. The selection of this particular image is driven by the fact that it does not contain any synthetic CME feature. The remnant star field signal (which arises from, e.g., the variation of the charge collection as the star moves across the CCD pixel boundaries) was suppressed by replacing those pixels with intensity exceeding three standard deviations from the mean intensity of a region (25 pixel radius) centered at the pixel, but excluding the pixel. The Solarsoft routine *sigma_filter* was used for that purpose. For illustration, the "cleaned" snapshots are shown in Figure 6.

To help compare, quantitatively, the recovered and the original synthetic CME signal, we plot in Figure 7 the intensity

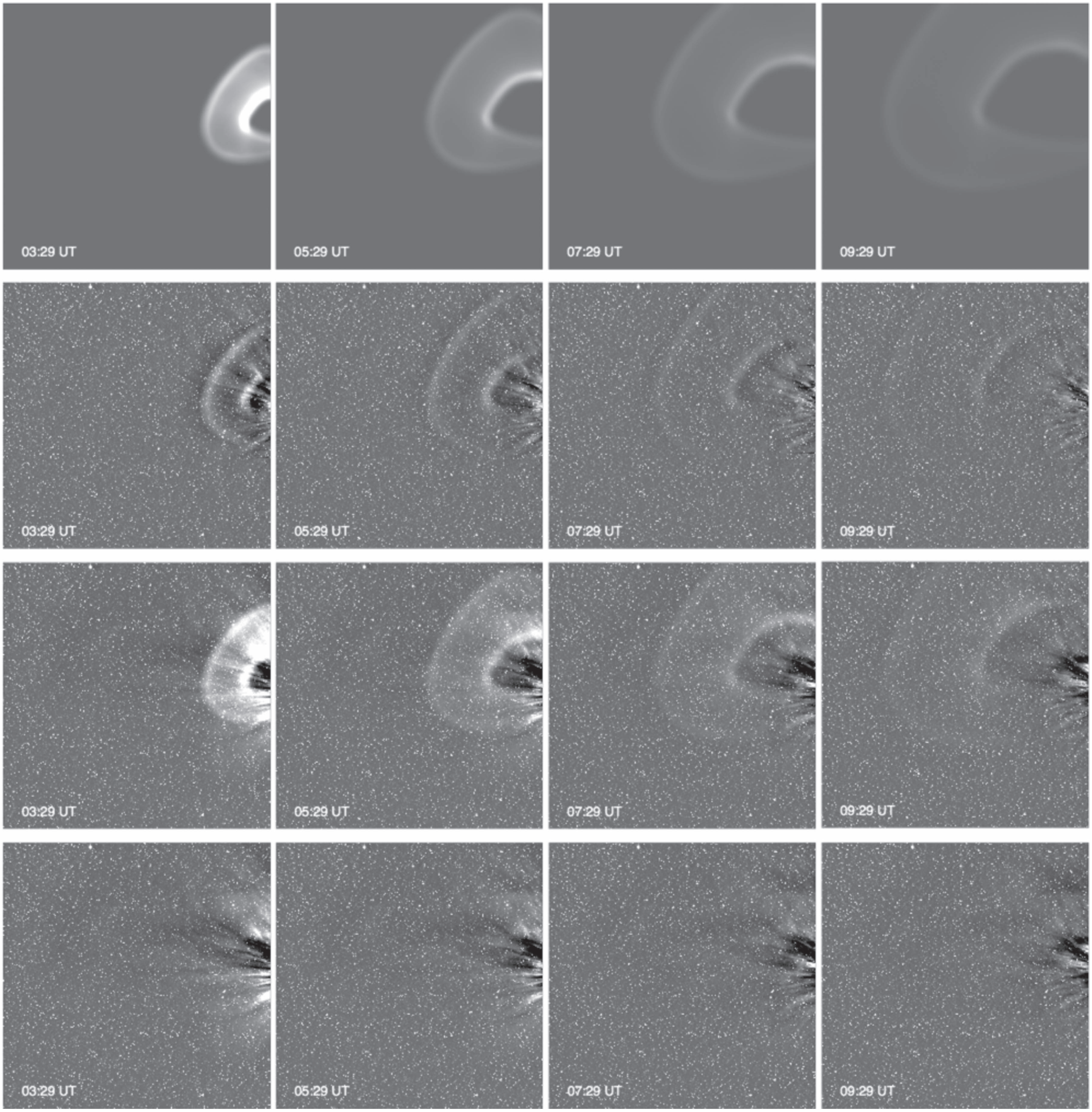

Figure 5. Photometric analysis. Top row: synthetic CME snapshots (S_t). Second row: excess brightness snapshots (B_t). Third row: snapshots of the excess brightness images B_t with the residual added (K_t). Bottom row: snapshots resulting from subtracting the synthetic CME S_t from K_t. All frames are in calibrated units, and shown intensity-scaled to $[-0.005, 0.01] \times 10^{11}$. For details, see the text.

profiles (S_t in black, B_t in red, K_t in green, and F_t in blue) of the four time instances depicted in Figure 6. We note in the figure that the recovered CME signal as given by K_t matches the original synthetic signal. The negative values, on the sunward side of the image, are the result of the subtraction of the pre-event image at 00:09 UT, demonstrating the dynamic nature of the coronal scene. It is clear, from the plots, that to reveal the K-coronal dynamic features, it suffices to remove the background scene as computed with our technique (relative percentage error $<0.5\%$). However, in order to fully recover the CME event, it is necessary to add the residuals (compare, e.g., the red and green curves).

4. Results

The individual background models of all *ST-A*/HI-1 images until right before the S/C crossing behind the Sun have been created with the state-of-the-art algorithm described here. The creation of the background models for *ST-B*/HI-1 is currently under way. We have selected several examples here to

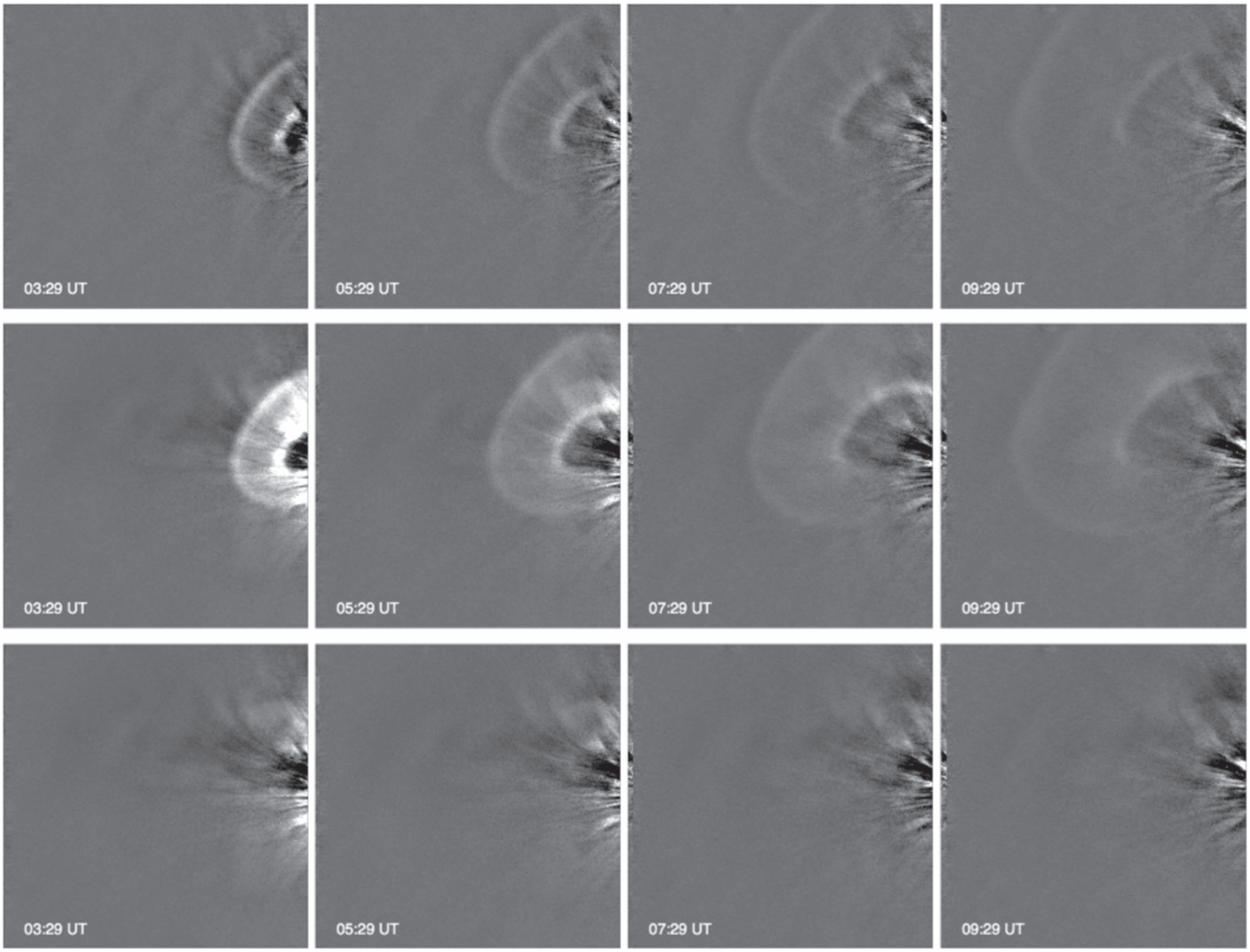

Figure 6. Photometric analysis. Same as the three bottom rows of Figure 5: the first frame of the test set (at 00:09 UT), shifted in the x direction to account for the star field displacement at the given time, has been subtracted from the corresponding snapshots. The resulting images have been filtered with a sigma filter to diminish the effect of the remnant signal of the star field. All frames are in calibrated units, and shown intensity-scaled to $[-0.005, 0.01] \times 10^{11}$. For details, see the text.

demonstrate the potential of our heuristic algorithm to provide new insights relating to (i) instrumental issues (Section 4.1), and (ii) the detectability of K-coronal features (Section 4.2).

4.1. Instrumental Issues

4.1.1. Camera Electronic Box Duty Cycle

We have analyzed in detail the full set of images taken by *ST-A*/HI-1 on 2011 June 25 to look for anomalies or artifacts that could have been introduced by our technique. On that day, 37 images were taken. The first image of the day was a single, full-resolution (2048×2048 pixels^2) image. Two minutes after the full-resolution image, the sequence of 36 images began, having been taken with a time cadence of 40 minutes under two different observation modes (keyword OBS_ID in the image headers, namely 1516 and 1518). Each *ST-A*/HI-1 image taken under OBS_IDs 1516 and 1518 is 2×2 binned aboard the S/C, and is obtained as the sum (aboard the S/C) of 30 short-exposure images, which have had the electronic bias subtracted and the effect of cosmic ray impacts removed. The electronic bias that is subtracted is the average of 2048 samples of the bias from an underscan pixel (one in each row) in the horizontal shift register of the CCD. However, the value that is subtracted is the integer formed from the average computed (and sent down to the ground) by dropping the fractional component. The effect of cosmic rays is computed by comparing each pixel to the previous image. If the difference is greater than five times the photon noise, then the pixel value is replaced by the value in the previous image. The background cosmic ray rate is about 6 photons $\mathrm{pix}^{-1}\,\mathrm{s}^{-1}\,\mathrm{cm}^{-2}$, so that without a solar particle storm, the number of pixels that are replaced depends on the number of seconds since the previous image. The same calibration procedure was applied to both observation modes.

A movie generated from the 36 calibrated images, each one normalized by its own background, shows no noticeable intensity flicker (not shown here). There is also no noticeable intensity flicker in the movie of running-difference of these background ratio images, regardless of the time lag between the images used to build the running-difference frames. This is demonstrating that the backgrounds are producing consistent image background subtractions. The lack of flicker is equivalent to differences of no more than 0.2 DN, or about 5 photons incident on the detector. This has been tested on many dates with the same result—no flicker is apparent.

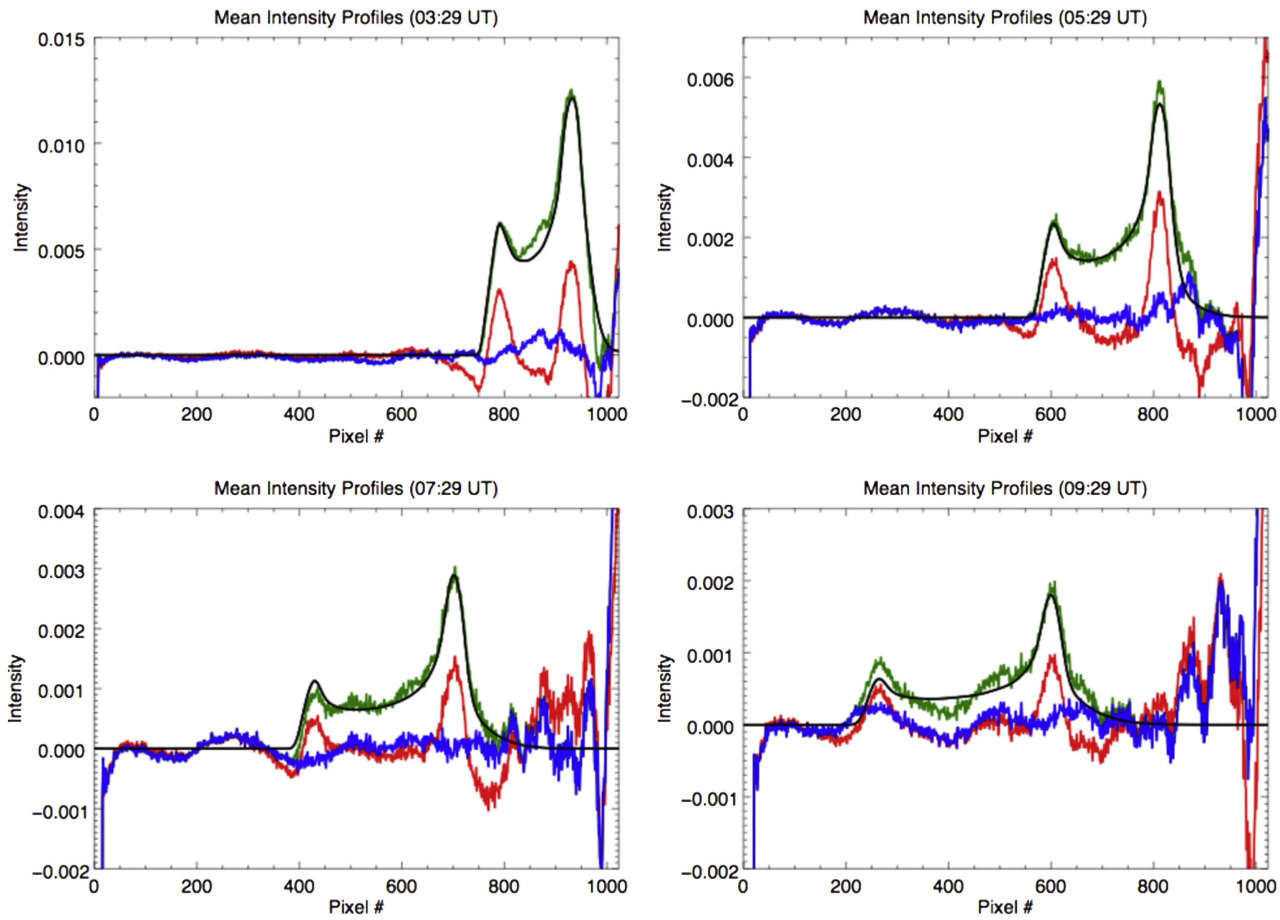

Figure 7. Photometric analysis: quantitative comparison. The different curves represent the intensity profiles as obtained by averaging the individual intensity profiles between rows 520 and 640 at each time instance defined in Figure 6. Black: synthetic CME (S_t); Red: excess brightness (B_t); Green: excess brightness with remnant signal added (K_t); Blue: difference between K_t and S_t. See the text for details.

As was shown in Section 2.3, there is some remnant K-coronal signal in the individual backgrounds. Therefore we constructed a single background out of the 36 individual backgrounds to minimize the effect of the residuals (e.g., a daily median). When the individual *ST-A*/HI-1 calibrated images were processed with that single background, we found that there was a slight flicker if the time lag between the images used to build the running-difference frames was not a multiple of 120 minutes. To discard the effect of an artifact introduced by the technique, we made running-difference movies with different time lags of level-05 uncalibrated *ST-A*/HI-1 images for the corresponding day. The intensity flicker effect is still present in the uncalibrated images. The effect is so subtle that we should have not detected it without knowing that it is indeed there. In a study of small-scale, periodic, solar wind density enhancements using *ST-A*/HI-1 data, Viall et al. (2010) also found periodic intensity fluctuations with a frequency of 0.139 mHz (120 minute) in every pixel analyzed, regardless of the presence/absence of a coronal feature. The authors did not find any apparent physical reason for this periodicity.

In the left panel of Figure 8, we show the intensity flicker as represented by the percentage variation of the de-trended mean intensity value of the individual background models of the 36 images under study (dashed line). The time instances of each observation mode are represented by the red asterisks (OBS_ID 1516) and green squares (OBS_ID 1518).

In examining the magnitude and source of the flicker, in the left panel of Figure 8, we overplot with the continuous black line the percentage variation of the mean bias value of the CCD camera (as reported in the header of the *ST-A*/HI-1 images). As can be inferred from the plot, the mean value of the bias also exhibits 120 minute periodicity, with a variation <0.1 DN. This variation is extremely low, justifying the flight software practice of subtracting the integer value. The standard deviation of the computation of the average bias for an individual image is on the order of 0.05 DN, indicating that within an image, the offset voltage generating the bias is quite stable.

To examine causality, we first checked if the bias evolution was correlated with the time variation of the intensity flicker. The Pearson correlation coefficient of the two signals is 0.75, increasing to 0.89 if the first and last five observations are discarded. It is not the objective of this study to elaborate on the reasons for this. Then we found that the camera electronics box (CEB) exhibits a ± 0.3°C cyclic variation over 120 minutes (see Figure 8, right panel). The CEB is where the offset bias is applied and the analog video is digitized. The Pearson correlation coefficient of the mean intensity flicker and the CEB temperature is only 0.39. However, the cross-correlation coefficient peaks at a time lag of 40 minutes (-0.89). The small cyclic variation and the high absolute value of the correlation coefficient between the CEB temperature and the offset bias indicates that the offset bias generation is sensitive to the CEB thermal variation. The fact that both signals are out of phase

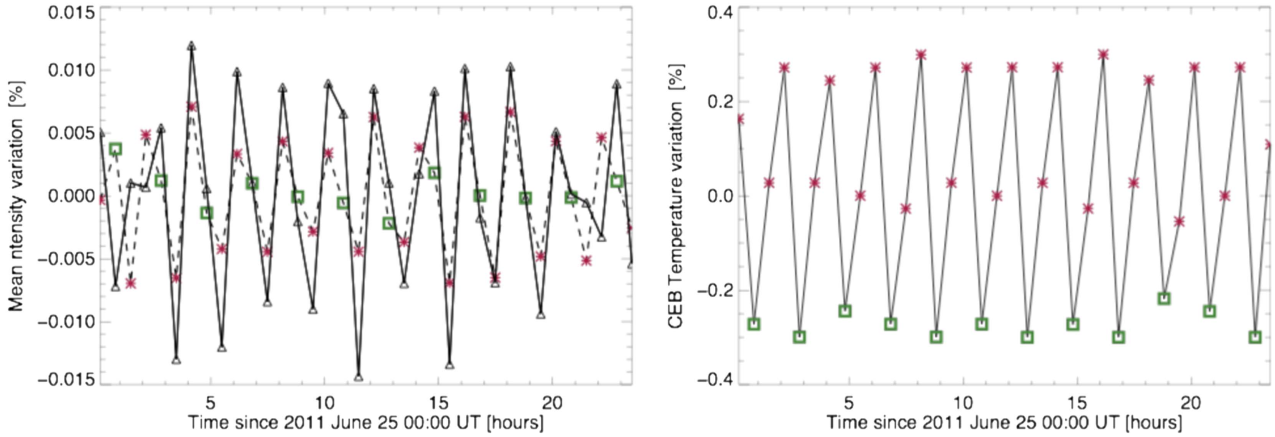

Figure 8. Instrumental Issues. Left panel: the dashed black line represents the variation of the mean intensity of the background models of the corresponding calibrated images taken by *ST-A*/HI-1 on 2011 June 25. The solid black line joining the triangle symbols depicts the CCD mean bias variation. Right panel: Camera Electronic Box (CEB) temperature variation. In both panels, the green squares and red asterisks are used to denote the observation mode (OBS_ID 1518 and OBS_ID 1516, respectively).

Figure 9. Sample frames of the NRL monthly standard background models normalized by the corresponding background models computed with our technique. The frames reveal (1) instrumental artifacts (left panel); (2) saturated, slow-moving features (middle panel); and (3) remnant pseudo-static coronal features and star tracks in the NRL standard background models (right panel). For details, see the text.

with a time lag of 40 minutes indicates that the CEB temperature decrease produces a bias increase later. The small temperature variation in the CEB is due in some unknown way to the power dissipation associated with the HI instrument operation within the 2 hr scheduling block. The analog-to-digital converter (ADC) that converts the analog video signal to a digital number (DN) does not appear to be sensitive to the CEB thermal variation, since there is no flicker in the background-corrected images.

We note that this effect was seen on any of the randomly selected days of *ST-A*/HI-1 mission we tested, and thus we conjecture that it is probably occurring for the entire mission.

4.1.2. Instrumental Artifacts

The NRL ST/HI-1 monthly background models (hereafter standard models) are created as the minimum of the daily median of ST/HI-1 images over a time period of 27 days. As an extra test to assess the reliability and consistency of our technique, we created monthly background models out of our individual background models in a similar fashion. Figure 9 shows three snapshots representing the ratio between co-temporal *ST-A*/HI-1 NRL standard models and ours for three different time periods in the year 2011.

Due to the characteristics of the technique devised, our background models do not include artifacts of instrumental nature with particular characteristics. Therefore the normalization of the standard models with our models should highlight these instrumental artifacts, as well as any other remnant signal between both such models. In particular, on the image in the left panel of Figure 9, we distinguish various intensity patterns that are instrumental in origin, identified by some arrows and dotted shapes on the frames to guide the eye when necessary. Namely, (i) a set of periodic circular saw marks extending all across the image (one such saw mark is pointed out with a green curved dotted line); (ii) two sets of periodic (very faint) parallel lines that cross at perpendicular angles extending all across the image (see, e.g., the dotted red cross); (iii) a big circular area of slightly different overall intensity (delimited by a dotted yellow circle), which can be better discerned in the image in the right panel; and (iv) faint and diffuse stripes (some pointed out by blue arrows). The first two sets of artifacts are the result of the fabrication of the camera detector. The third one is the boundary of vignetting caused by the field stop. The fourth set is a constant feature in

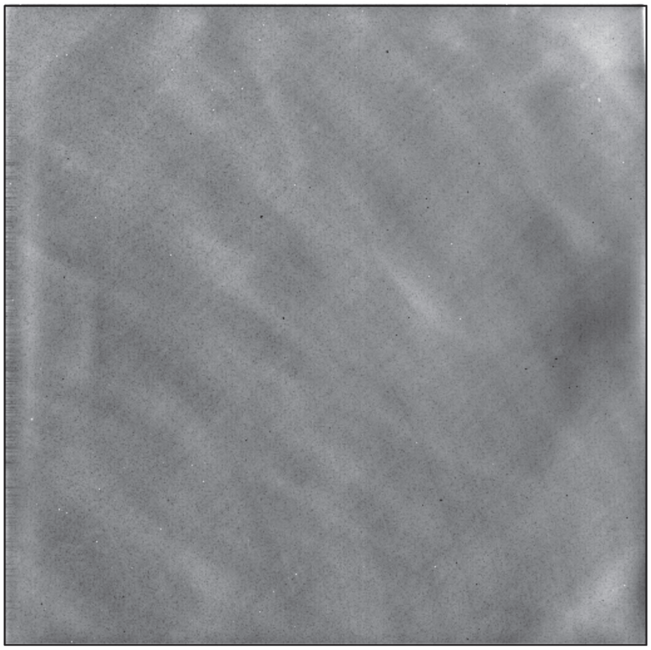

Figure 10. Empirical model of the instrumental artifacts obtained as the annual median of the normalized NRL monthly standard background models for the year 2011 (see Figure 9).

the images, which we believe results from the fabrication process of the CCD, but the specific cause is not obvious to us.

On the image in the middle panel of Figure 9, we see a set of white vertical stripes, which appear saturated in the intensity scale used. They are present only during some time periods in the standard models. The vertical stripes arise from the passage of saturated planets (Venus and Mercury) through the field. The vertical length is caused by the shutterless readout. The spacing between the stripes results from the way in which the background models are created (a monthly minimum of the daily medians).

It is a well-known problem that the background images during solar minima are contaminated with pre-existing streamers, because they are persistent at the same latitude for the entire month. This issue, however, can be true at any time: if K-coronal structures persist during an extended time frame in a given 27 day period (e.g., a long-lived streamer or a planet), the corresponding standard background model will be contaminated with a remnant signature of the feature. This can be seen in the right panel of Figure 9 (pointed out by green arrows). Likewise, a remnant signal of the star field displacement in the 27 day period selected to create the standard backgrounds models also show up (see, e.g., the almost horizontal short lines on the upper left corner of the frame). Both features have intensity levels greater than that of the background intensity. This fact indicates that the feature is a remnant structure more prominent in the standard models than in ours.

Inspection of the time sequence of the normalized standard models comprising the whole year 2011 shows that the pattern arising from instrumental issues (left panel of Figure 9) persists in time. The time median of this 1 year set is shown in Figure 10, where the instrumental pattern mentioned previously can be seen. This median image can be considered for practical purposes the empirical model of the instrumental artifacts. (This empirical model is the one used to help obtain the snapshot shown in the bottom right panel of Figure 4.) Re-normalization of the previous background ratio images by this median image removes the steady artifacts. In Figure 11 we show the three frames of Figure 9 normalized by the instrumental artifact image (see Figure 10). The remnant K-coronal structures and/or star tracks that contaminate the standard models are enhanced as a result.

In summary, the instrumental artifacts of ST/HI-1 were revealed by normalizing the standard models with the background models created with this new technique. Since the artifacts are present in every image, they can now be easily generated and removed.

4.2. Identifying Coronal Structures

The main advantage of the technique devised is that only the image to be treated is necessary to create a background intensity model. By removing/normalizing the intensity background, it is then possible to combine images taken from different viewpoints because of, for example, S/C orientation (Section 4.2.1) or time lag (Section 4.2.2) between observations.

4.2.1. S/C Rolls

As part of the on-orbit calibrations, the *STEREO* spacecraft perform rolls about the solar vector. This procedure is very effective in enabling the determination of the stray-light performance in the SECCHI coronagraphs. At various (i.e., 8) roll angles, the S/C would pause and allow SECCHI to collect a set of images. The usual procedure to determine the stray light consists of differencing images taken 180° apart after rotating one of the images by 180°. By assuming that the corona has not changed significantly in the short time between the two sets of observations, the difference then reveals the non-radially symmetric stray-light pattern of the SECCHI coronagraphs without knowing the background. Although this technique was not useful to determine the stray light of the heliospheric imagers, because of their off-axis FOV, we were able to apply our technique to each of the corresponding *ST-A*/HI-1 images obtained at each roll position to reveal a new view of the corona. This was performed for all of the roll maneuvers.

Figure 12 (left panel) shows the resultant composite image of the individual background models for the calibration rolls taken on 2011 July 26. The composite snapshot shows the extension of the F-corona into the zodiacal light. We notice an asymmetry of the emission on the western hemisphere, associated to the distortion of the resulting respective frame after the coordinates transformation. We believe this effect is due to a slight error in the instrument parameters used in the World Coordinates System (WCS; Thompson 2010). (Note the different size of the frame centered in the equatorial plane on the right side of the image.)

On the right panel of Figure 12, we show the composite of the corresponding background-corrected calibration rolls. This composite shows two CME events in progress on opposite sides of the Sun. Multiple CMEs is not unusual in the coronagraph images, but the 360° view of the interplanetary space between 4° and 24° elongation has never been seen before in the ST/HI type of instrument. Note that to reduce the effect of the star field, the Solarsoft *sigma_filter* routine was applied. Moreover, as shown in Section 4.1.2, the time median of the background-corrected frames can be used as a model of

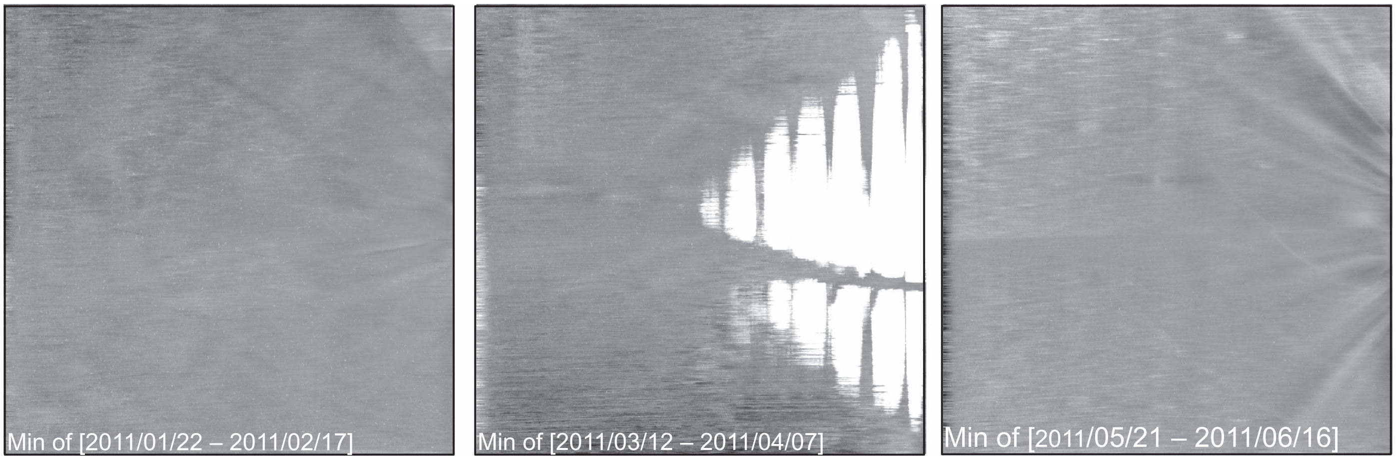

Figure 11. Sample frames of the normalized NRL monthly standard backgrounds models in Figure 9, corrected by the empirical model of the instrumental artifacts (see Figure 10).

the instrumental artifacts. Therefore, to obtain the frames free of instrumental artifacts, each frame was normalized (prior to the coordinates transformation) by the time median of the corresponding background-corrected frames obtained for the six roll sets taken during the year 2011 (i.e., on February 01, April 05, May 03, July 26, October 26, and November 29).

4.2.2. Early Development of Co-rotating Density Structures

Sheeley et al. (2008a) first reported the presence of density structures co-rotating in the field of view (FOV) of ST/HI-2 instruments. Later on, Sheeley et al. (2008b) interpreted these structures as "density compressions that are driven radially outward by high-speed streams from coronal holes" (i.e., co-rotating interaction regions, hereafter CIR; e.g., Lee 2002). Rouillard et al. (2008) provided the first evidence of the formation of a CIR in the *ST-A*/HI-1 FOV. More recently, Plotnikov et al. (2016) presented a catalog of co-rotating density structures observed in the FOV of the *ST-A* heliospheric imagers between 2007 April and 2014 August. The catalog was built upon the analysis of elongation-time plots (or J-maps; Sheeley et al. 1999) created from running-difference images. Although the visualization and analyses of these structures is facilitated with the use of J-maps, their development and full extent in the ST/HI-1 FOV is still not obvious (see, e.g., Figure 2 in Rouillard et al. 2008). In this section, we show a second example of the usefulness of the heuristic approach, developed to reveal and enhance the contrast of these faint co-rotating structures.

Figure 13 (top row) shows four time instances of the development of a CIR (pinpointed by white arrows) that was observed in the FOV of the *ST-B*/HI-2 instrument between 2007 December 15 and 17 (our assertion of its nature is supported by its resemblance with the features observed in, e.g., Figures 2 and 4 in Sheeley et al. 2008b). Each snapshot results from the difference with a prior image (time lag of 120 minute), after shifting the base image in a given amount of pixels to match the average displacement of the star field. In addition, the Solarsoft routine *sigma_filter* was applied to reduce the effect of the remnant point-like, undesired features. The oval-shaped mask on the right of each snapshot is intended to reduce the intensity flickering arising from the presence of Earth at the border of the occulter.

Figure 13 (bottom row) shows four snapshots of a *ST-B*/HI-1 time sequence obtained in a time period prior to the appearance of the CIR in the *ST-B*/HI-2 FOV. Briefly, each snapshot was obtained as $I_t - I^s_{t-k} + R_t$, where I denotes a "processed" *ST-B*/HI-1 calibrated image, and R_t the residual between the two "processed" calibrated images. The subindexes t and $t - k$ point to the time instances of each image used to obtain the corresponding difference frame (k denotes the time lag), and the superscript s indicates that the base image has been shifted to match the star field of I_t before subtraction.

To process each *ST-B*/HI-1 calibrated image, we follow the scheme already detailed in previous examples. Namely, we first normalized each calibrated image by its own background model, as created with our technique (hereafter background ratio images). As aforementioned, this operation enhances instrumental artifacts. As we have not yet processed a full year of *ST-B*/HI-1 data to create a model of the instrumental artifacts as detailed in Section 4.1.2[1], we built an approximate model of the instrumental artifacts by taking the time median of the set of background ratio images in a 2 days time period (2007 December 14–15). Next, we renormalized the background ratio images with this empirical model to minimize their effect (we call the resulting images I_t).

We proceeded then to make the running-difference snapshots by subtracting from each "processed" image I_t a base image taken 240 minutes earlier (I^s_{t-4hs}). The base image I^s_{t-4hs} was shifted a sufficient number of pixels to match the star field in I_t (the star field displacement was calculated by computing the maximum of the cross-correlation of the corresponding two background ratio images used to create the given difference snapshot). The Solarsoft *sigma_filter* routine was applied to the difference to eliminate remnant point-like features arising from, for example, the variation of the charge collection as the star moves across the CCD pixel boundaries that results in an incomplete cancellation of the star field after shifting. Finally, the corresponding residuals (computed as specified in Section 2.3) were added.

The white arrows in the bottom row of Figure 13 point to a feature whose location and timing in the *ST-B*/HI-1 FOV agree well with the development of the CIR observed in *ST-B*/HI-2

[1] We believe, however, that the creation of such a model for *ST-B*/HI-1 using a very extended period of time (as it was the case for *ST-A*/HI-1) may have problems due to the jitter in the pointing of *ST-B*/HI-2.

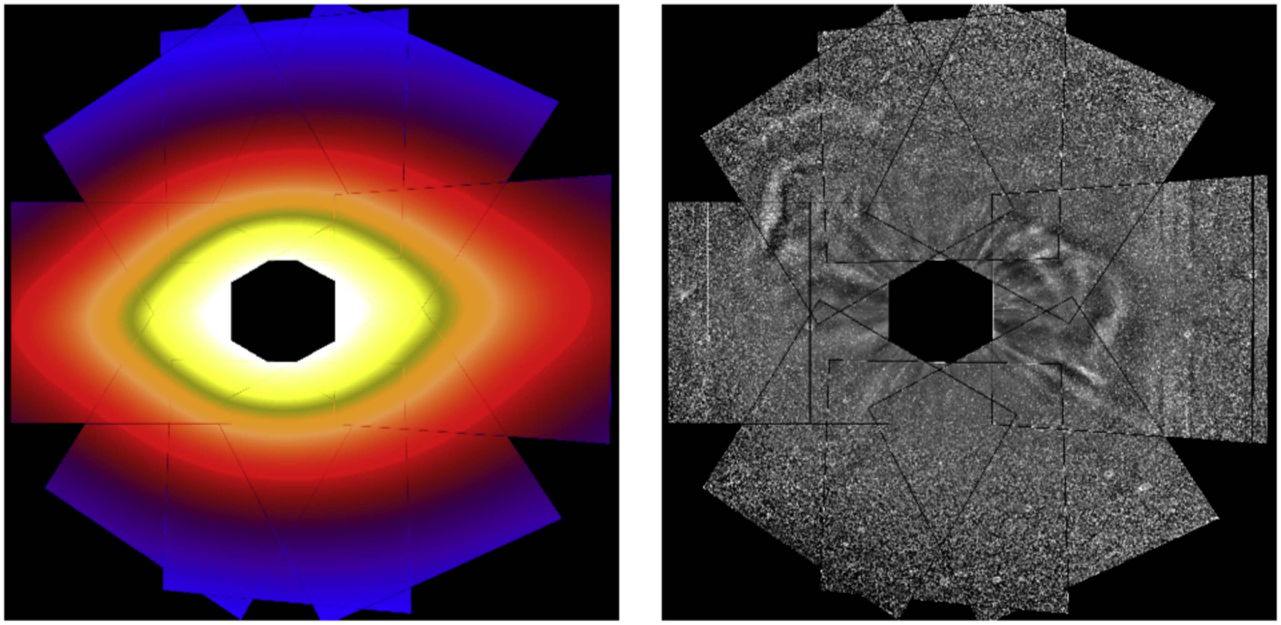

Figure 12. Reconstruction *ST-A* roll on 2011 July 26. Left panel: 360° view of the zodiacal light (in logarithmic scale). Right panel: 360° view of the interplanetary space around the Sun exhibiting the development of two dynamic, K-coronal features.

images. Moreover, the feature extends all across the vertical extension of the FOV of the instrument, appearing slightly inclined. This inclination matches the inclination exhibited by the CIR in the *ST-B*/HI-2 images. The shape of this feature (i.e., a linear segment) is presumably reflecting the shape of the leading edge of a coronal hole and the compression caused by the high-speed stream running into the higher density, low speed stream. Therefore, we conjecture that this feature is a likely signature of the early development of the co-rotating structure later observed. The complexity of the coronal scene at very small elongations made difficult the clear identification of the feature formation presented in this example. An in-depth analysis is beyond the scope of this paper.

5. Discussion

The original impetus for this effort was to develop a technique that could determine the intensity background of a heliospheric imager from a single image, with the ultimate aim of devising an adaptable scheme to reveal the K-coronal features, even in the presence of rapidly changing background scenes. In this paper, we have described and assessed the technique as implemented to create individual background intensity models out of single ST/HI-1 images, and presented some key examples. The success of the algorithm relies on (1) the use of a couple of different techniques to filter out the desired frequencies and/or correct the bad fitting of the chosen analytical models, and (2) the switch to the gradient space to avoid the large intensity gradient between the inner and outer edges of the FOV of the ST/HI-1 images. Artifacts introduced along the way are self-consistently minimized by the algorithm. The availability of such background models allows us to develop the best strategy to tackle unforeseen situations.

In our application, the technique helped reveal small variations in the detector such as (1) overall intensity variations due to the duty cycle of the camera electronic box (Section 4.1.1), (2) pixel-to-pixel variation resulting from manufacturing imperfections (Section 4.1.2), and (3) diffuse regions of enhanced emission presumably due to stray-light artifacts (Section 4.1.2). This preliminary work has given us confidence that long-term treatments of the backgrounds will result in better representation of the background with less remnant K-coronal structure and excellent instrumental artifacts. These will result in better calibration.

As demonstrated in Section 4.2.1 for the generation of backgrounds for the SECCHI calibration rolls, this technique would be ideal for coronagraph telescopes or heliospheric imagers in low Earth orbit. Such telescopes often have variable stray-light patterns due to the variable orientation of the instrument with the atmosphere. This technique has proven to be very sensitive and, we believe, would easily identify the variations of the stray light as a function of the orientation. The construction of the 2D images of the zodiacal light was quite startling to us, which performed as a function of the heliocentric distance, would show the flattening of the zodiacal light ellipse. A regular campaign of such images might show temporal changes in the zodiacal light associated with comets or asteroids.

The individual background models are, however, not perfect: some remnant K-coronal signal still contaminates them (see, e.g., Sections 2.3 and 3). In all cases tested during the present study, the residual intensity variation due to the passage of bright events never exceeded 1%. Moreover, there is a slight intensity variation from row to row (≈0.1% at very large elongations for *ST-A*/HI-1) resulting from the individual treatment of each row. The latter, however, does not visually contaminate the final products (see, e.g., Figure 4 panel (e); third and second rows of Figures 5 and 6, respectively; and the right panel of Figure 12). Due to the problems with the pointing of *ST-B*, however, this variation slightly affects the running-difference-based products, although the effect does not preclude the revealing of extremely faint features (see, e.g., the bottom row of Figure 13). In spite of all this, our heuristic approach proved to be a very powerful methodology for revealing both small density inhomogeneities

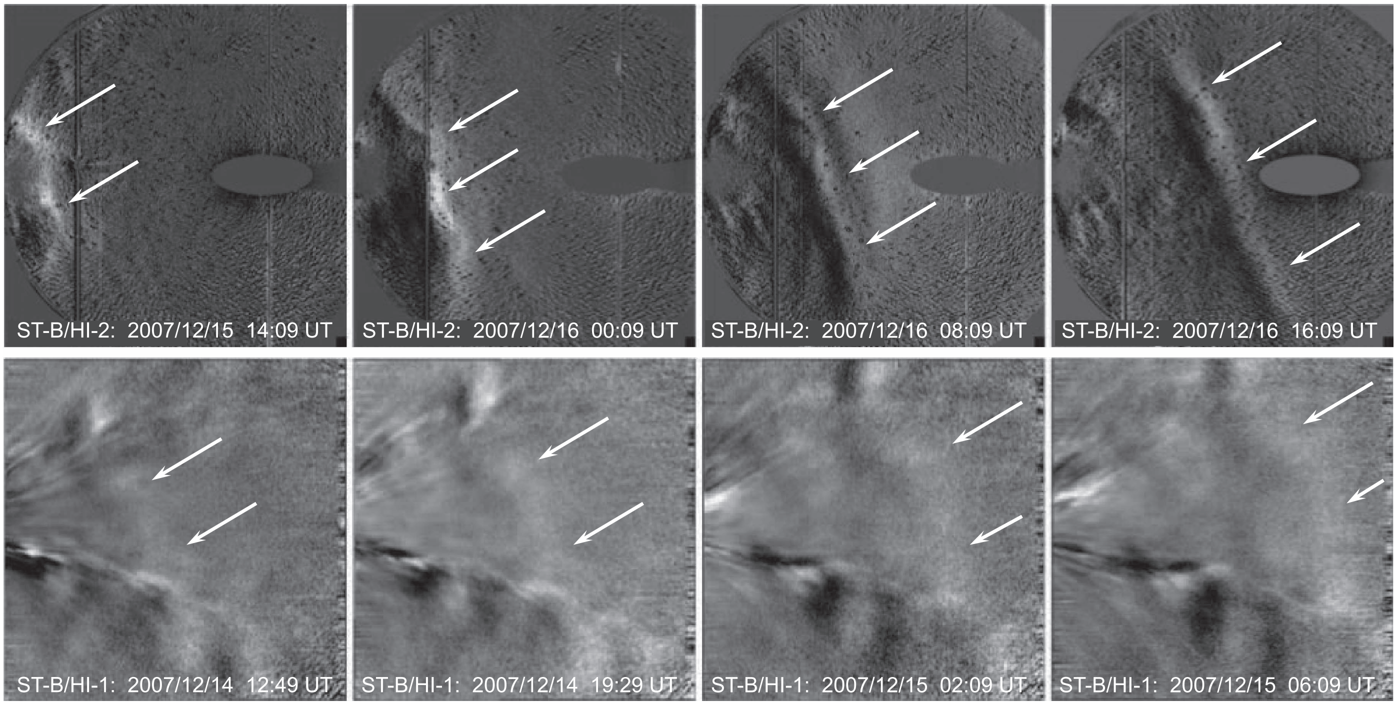

Figure 13. Illustration of the development of a co-rotating density structure. Top row: running-difference snapshots of *ST-B*/HI-2 images (time lag: 120 minute), base image shifted to account for the star field displacement. Bottom row: "processed" *ST-B*/HI-1 running-difference snapshots (time lag: 240 minute), base image shifted to account for the star field displacement. The arrows point to the co-rotating density structure.

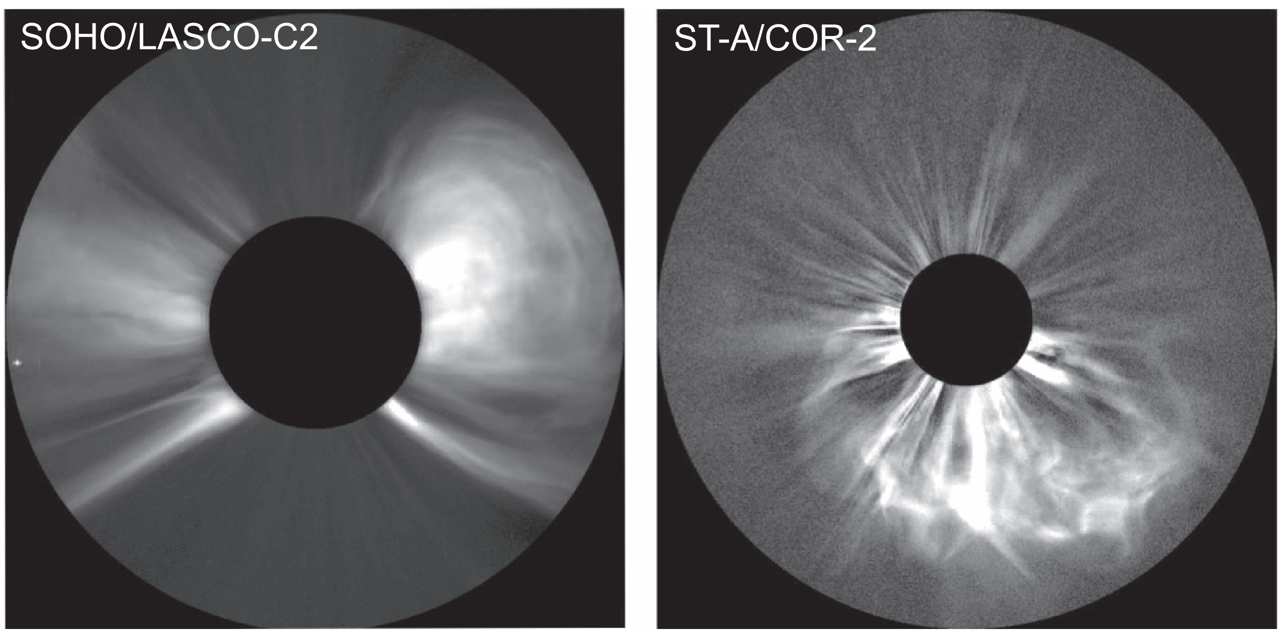

Figure 14. Left panel: *SOHO*/LASCO-C2 background ratio image (1998 May 06 at 09:02 UT). Right panel: *ST-A*/COR-2 background ratio image (2012 June 12 at 07:24 UT). The corresponding background model used to obtain both images has been computed as the minimum of the daily median of the individual background models in a 27-day time period. The individual background models have been created with a technique akin to the one presented in this paper.

and faint, large-scale density structures in the presence of a high stable background. In the coronal images shown in this work, there is a large intensity gradient in the images, which is largely removed by the initial ad hoc function (i.e., the analytical model chosen), while the residuals to the ad hoc function are consistently reduced with higher order corrections. In another application, a different function can be used, but the succeeding steps would be virtually identical. For example, the success of this heuristic approach presented here led us to adapt it to coronagraph images such as from *SOHO*/LASCO-C2 and SECCHI/COR-2. Examples are shown in Figure 14. Details of the customized algorithm to create individual backgrounds models for white-light coronagraph data will appear elsewhere.

In the following, we briefly put in perspective its usefulness to present and upcoming missions, and reflect on its advantages and limitations.

5.1. On the Applicability to the STEREO/HI-1 Beacon Mode Data

The data provided by the *STEREO*/SECCHI instruments are downlinked to the ground in two modes: full science data and quick-look "beacon mode" data. The beacon mode (highly compressed images) provides data in near real-time for space weather purposes. As in the full ST/HI-1 science data, the subject of interest for space weather purposes (i.e., the dynamic coronal transients such as CMEs), is hidden by the brighter background of the image. Therefore the standard procedure to reveal the white-light transients in near real-time is to create running-difference frames. However, as shown in some of the examples presented previously, the running-difference approach also enhances the background star field, making it difficult to follow faint transients. This can be circumvented by shifting the base image a certain amount of fractional pixels to match the star field in both images. However, in the case of ST/HI-1 images, this trick will introduce an undesired artifact resulting from the unmatched background intensity distribution (see Section 2.3 and Figure 4).

By normalizing each image with a standard model of the intensity background before shifting, the problem arising from the unmatched background intensity distribution can be avoided. However, for beacon data, for example, these background models do not actually exist. One alternative is to use a median of a set of previous images to get a near real-time model of the background intensity, but the potential presence of big point-like objects in the scene (e.g., a planet) may introduce artifacts in this background (see, e.g., Section 4.1.2 and the middle panel of Figure 9). Moreover, the potential presence of a bright coronal dynamic transient in the time frame used to create the median image representative of the background will also introduce undesired artifacts. All these issues become inconsequential with the use of individual background intensity models, as was shown, for example, with the examples presented in Section 4.2.

5.2. On the Applicability to the Low Latency of SolO/SoloHI and SPP/WISPR

The SolO and SPP missions are both planned to have perihelia inside of the orbit of Mercury, closer than any man-made object has ever gone. Their orbits are such that the full-resolution data may take over a year to be sent to the ground, because the S/C are on the other side of the Sun from Earth, and possibly obscured from Earth. Thus the concept of low-latency data transmissions has been proposed to greatly reduce the number of bits that would be sent down to the ground. For the SolO/SoloHI and SPP/WISPR instruments, this means that highly compressed images or subsets of the images would be sent to the ground soon after they were taken in a similar fashion as the *STEREO* beacon mode. In this mode, perhaps only one image can be sent to the ground every one or two days. The technique described in this paper will be essential to reveal the dynamical nature of the solar wind from these intermittent observations to give an early indication of what these new regions of space are like and how different they may be from our expectations.

Moreover, the generation of individual image backgrounds will be essential to properly scale the science data, as the orbits characteristics of these two missions will preclude the creation of backgrounds using extended periods of time. We firmly believe that the approach exposed in this paper will be useful to identify the region where the dust begins to evaporate due to solar heating and therefore not contribute to the F-corona. Such a zone was postulated to exist by Russell (1929) at 4–5 $R_{\odot}$. Depending on the pyrolytic properties of the dust grains, the interplanetary dust will evaporate at different heliocentric distances. For example, grains of magnatite, amorphous olivine, or quartz could start to evaporate as early as 40 $R_{\odot}$, 15 $R_{\odot}$, and 4 $R_{\odot}$, respectively (Mann et al. 2004). These are idealized dust grains, so the actual distances of evaporation may be quite different. R. A. Howard et al. (2017, in preparation) have been studying the visibility of the dust-free zone in the two white-light imagers of these missions (i.e., SolO/SoloHI and SPP/WISPR). With the technique presented in this work, the regions where the evaporation starts to occur will likely be revealed on the data of these two upcoming missions.

5.3. The Technique's Concept in a Nutshell: Pros and Cons

In any real application, the physical nature of the observed scene precludes the determination of the real background. Any approach to obtain the backgrounds will then provide just a proxy, whose degree of accuracy will matter upon the objective pursued. In particular, our technique basically resembles the functioning of a multi-resolution low-pass filter, selectively filtering out high-frequency spatial scales up to a certain order. The order up to which features can be filtered out will depend on the size and type of kernel, plate scale of the instrument, and extent of the instrument's FOV. In this way, the net effect is to high-pass filter the F-coronal structures in the image plane.

Therefore, our technique has a cost: the individual backgrounds created to remove the smooth, slow-varying brightness also take out part of the desired K-coronal signal. But, at the expense of losing some signal, we are able to subtract prior instances of the scene not close in time without the perturbation introduced by (1) the displacement of the star field, and (2) the variation of the F-corona resulting from the change of perspective after correcting by the star field shift. As shown in this work, the limitation exposed previously is inconsequential for ST/HI-1-like instruments (i.e., instruments in a slow-varying orbit observing an almost constant portion of sky); in this case, it is overcome by adding the differential remnant signal present in the background models). Moreover, since the contribution of the K-coronal signal to the total brightness is largely reduced in the individual background models, the standard time-dependent background models obtained for ST/HI-1-like instruments can be greatly improved by creating them from the individual background models rather from the images themselves.

There is, however, a couple of sources that adversely affect the creation of our background models: (1) the passage of a very bright object (e.g., Venus, Mercury, or a big comet), and (2) an extended celestial feature (e.g., the Milky Way). The spatial size and the CCD bleeding of a saturated signal from the former source limits the ability of the technique to fully filter it out, resulting in artifacts in the corresponding models. As for the latter, the spatial scale of the cloud-like appearance stemming from the high density collection of stars along the line of sight is close to the scale of the signal intended to be filtered out. As a result, the corresponding backgrounds can be contaminated (this is also true for techniques in the time domain).

6. Conclusions

We have developed a novel concept to model the white-light background intensity of individual ST/HI-1 images based on only the spatial characteristics of the background scene, ignoring the time domain. Time domain approaches exploit the stability of the dust distribution around the Sun. However, as the background scene depends on the observing point, time domain approaches fail or are not applicable in the absence of long observing sequences of the same portion of the sky. In contrast, our method harnesses (1) the smooth monotonic decrease with heliocentric distance of the F-corona; and (2) the known "break" in spatial scales between the K-coronal features of interest and the broad contributions from both the F-corona and stray-light elements of the background. Since the K-corona itself exists on a range of spatial scales that overlaps with the range occupied by the background, our method wipes a little off some K-coronal structures. Therefore, the cost of this completely non-time-dependent method is that the separation between background and signal of interest is not as clean as it would be with a time-dependent method (provided the necessary time sequence of observations exists to provide that model). But, on the other hand, it provides a means to obtain proxies of the background models in the absence of favorable observations.

As demonstrated in this paper, and in spite of the caveats mentioned previously (e.g., the method would not work when the spatial scale of the foreground structures is of the order of the background), our technique does an excellent job and helps improve the scientific return of the data. We believe that this concept has applicability to many other physical systems, and we have applied it to several types of coronal images. It does require some care in applying it to a new type of data—in the choice of the first guess of the model, the choice of the kernel size, and so on. But it is robust, having been run on thousands of images from the first $\sim$10 years of the *STEREO* mission with no or little supervision.

In summary, the heuristic approach presented here is an advance in the state of the art, and represents a leap forward both from an operational point of view, and from its versatility to reveal hidden features (both instrumental and physical). We invite the community to contact the authors to request more details on the technique or solicit the processing of particular data sets for specific scientific purposes.

The SECCHI data are courtesy of *STEREO* and the SECCHI consortium. The *STEREO*/SECCHI data are produced by a consortium of NRL (USA), LMSAL (USA), NASA/GSFC (USA), RAL (UK), UBHAM (UK), MPS (Germany), CSL (Belgium), IOTA (France), and IAS (France). The *SOHO*/LASCO data used here are produced by a consortium of the Naval Research Laboratory (USA), Max-Planck-Institut für Aeronomie (Germany), Laboratoire d'Astronomie (France), and the University of Birmingham (UK). *SOHO* is a project of international cooperation between ESA and NASA. We acknowledge the support from the NASA *STEREO*/SECCHI (S-13631-Y), SOC/SoloHI (NNG09EK11I), and the NASA/SPP/WISPR (NNG11EK11I) programs and the Office of Naval Research. We are grateful to Paul Landini (summer student under the 2016 Naval Research Enterprise Internship Program, NREIP), for his help in processing the *STEREO*/HI-1 background models. We thank Robin C. Colaninno for her assistance in suggesting and providing the CME synthetic model.

References

Billings, D. 1966, A Guide to the Solar Corona (New York: Academic)
Brueckner, G. E., Howard, R. A., Koomen, M. J., et al. 1995, SoPh, 162, 357
DeForest, C. E., Howard, T. A., & McComas, D. J. 2012, ApJ, 745, 36
DeForest, C. E., Howard, T. A., & Tappin, S. J. 2011, ApJ, 738, 103
DeForest, C. E., Plunkett, S. P., & Andrews, M. D. 2001, ApJ, 546, 569
Domingo, V., Fleck, B., & Poland, A. I. 1995, SSRv, 72, 81
Eyles, C. J., Harrison, R. A., Davis, C. J., et al. 2009, SoPh, 254, 387
Fox, N. J., Velli, M. C., Bale, S. D., et al. 2016, SSRv, 204, 7
Habbal, S. Rifai, Morgan, H., Druckmüller, M., et al. 2013, SoPh, 285, 9
Howard, R. A. 2006, in Solar Eruptions and Energetic Particles, Vol. 165, ed. N. Gopalswamy, R. Mewaldt, & J. Torsti (Washington, D.C.: American Geophysical Union), 7
Howard, R. A., Moses, J. D., Vourlidas, A., et al. 2008, SSRv, 136, 67
Howard, R. A., Vourlidas, A., Korendyke, C. M., et al. 2013, Proc. SPIE, 8862, 88620H
Howard, T. A., & DeForest, C. E. 2012, ApJ, 746, 64
Kaiser, M. L., Kucera, T. A., Davila, J. M., et al. 2008, SSRv, 136, 5
Koutchmy, S., & Lamy, P. L. 1985, in IAU Coll. 85, Properties and Interactions of Interplanetary Dust, ed. R. H. Giese & P. Lamy (Dordrecht: D. Reidel), 63
Lee, M. A. 2002, JGR, 105, 10491
Leinert, Ch., Bowyer, S., Haikala, L. K., et al. 1998, A&AS, 127, 1
Mann, I., Kimura, H., Biesecker, D. A., et al. 2004, SSRv, 110, 269
Morgan, H., Byrne, J. P., & Habbal, S. R. 2012, ApJ, 752, 144
Morgan, H., & Druckmüller, M. 2014, SoPh, 289, 2945
Morgan, H., & Habbal, S. R. 2007, A&A, 471, L47
Morgan, H., & Habbal, S. R. 2010, ApJ, 711, 631
Morgan, H., Habbal, S. R., & Woo, R. 2006, SoPh, 236, 263
Morrill, J. S., Korendyke, C. M., Brueckner, G. E., et al. 2006, SoPh, 233, 331
Mueller, D., Marsden, R. G., St., Cyr, O. C., et al. 2013, SoPh, 285, 25
Plotnikov, I., Rouillard, A. P., Davies, J. A., et al. 2016, SoPh, 291, 1853
Ragot, B. R., & Kahler, S. W. 2003, ApJ, 594, 1049
Rouillard, A. P., Davies, J. A., Forsyth, R. J., et al. 2008, GeoRL, 35, L10110
Russell, H. N. 1929, ApJ, 69, 49
Savitzky, A., & Golay, M. 1964, AnaCh, 36, 1627
Sheeley, N. R., Jr., Herbst, A. D., Palatchi, C. A., et al. 2008a, ApJL, 674, L109
Sheeley, N. R., Jr., Herbst, A. D., Palatchi, C. A., et al. 2008b, ApJ, 675, 853
Sheeley, N. R., Jr., Walters, J. H., Wang, Y.-M., et al. 1999, JGR, 104, 24739
Stenborg, G., Vourlidas, A., & Howard, R. 2008, ApJ, 674, 1201
Thompson, W. T. 2010, A&A, 515, A59
Viall, N. M., Spence, H. E., Vourlidas, A., & Howard, R. A. 2010, SoPh, 267, 175
Vourlidas, A., Howard, A., Plunkett, S. P., et al. 2013, Proc. SPIE, 8862, 88620I
Vourlidas, A., Howard, A., Plunkett, S. P., et al. 2016, SSRv, 204, 83
Wood, B., & Howard, R. A. 2009, ApJ, 702, 901